In-Flight Vibrations and Their Effects on Wing Mounted VHF Antennas

Matthew Turner[1] and Emily Arnold[2]
University of Kansas, Lawrence, Kansas, 66045

Airborne ice-sounding radars typically operate in the low-to mid-VHF spectrum. Most ice sounding missions require large cross-track arrays to reduce clutter from rough surfaces, necessitating antennas to be mounted on aircraft wings. The mechanical response of the airframe can affect the radar system performance due to the displacement and vibrations of both the wing and the antennas. This paper investigates the vibrational response of wing-mounted 70 MHz antennas developed by the Center for Remote Sensing and Integrated Systems (CReSIS) at the University of Kansas. A finite element model validated with experimental measurements is used to predict the antenna response in flight. From an analysis of the radar data from a recent flight test, it is apparent the airframe vibrations due to the engine are observed in the signal. Future study is recommended to further characterize this effect including impacts on beam forming and means to mitigating the response.

I. Nomenclature

ASD	=	amplitude spectral density
BPF	=	blade passage frequency
Ch.	=	channel number
CReSIS	=	Center for Remote Sensing and Integrated Systems
DAQ	=	data acquisition
FEM	=	finite element model
FFT	=	fast Fourier transform
FRF	=	frequency response function
PSD	=	power spectral density
UAS	=	unmanned aerial system
VHF	=	very high frequency

II. Introduction

Airborne radar remote sensing has a breadth of applications for earth observations. Many of these applications, such as land subsidence, soil moisture, snow depth and biomass typically operate well above the Very High Frequency (VHF) spectrum (30-300 MHz). Given that the size of a radar antenna is generally inversely proportional to its operating frequencies, these antenna systems can typically be installed in a single nadir port or pod. In such installations, the effects of the flexible and vibrating airframe are more negligible and can often be mitigated with carefully designed vibration mounts.

In the case of ice sounding applications, the operational frequencies are typically in the low- to mid-VHF spectrum [1-5]. Further, large cross-track arrays (direction perpendicular to flight) are advantageous for reducing clutter from rough ice surfaces which results in antenna elements being mounted to the wings. In these cases, the mechanical response of the airframe due to either the engine or blade passage frequency (BPF) may be of more significance [6]. The Center for Remote Sensing and Integrated System (CReSIS) at the University of Kansas has a long history of developing and integrating ice-penetrating radar systems for ice sounding applications. In this paper, we will examine

[1] Graduate Research Assistant, Department of Aerospace Engineering, 2120 Learned Hall, AIAA Student Member.
[2] Associate Professor, Department of Aerospace Engineering, 2120 Learning Hall, AIAA Associate Fellow.

the vibrational response of wing-mounted 70 MHz antennas that have been designed to integrate onto a Group III Unmanned Aerial System (UAS) that has a wingspan of less than 40'. Simulated mechanical responses are compared to experimental results. Further, radar data will be examined to assess the effects of the mechanical vibrations on the radar signal and antenna performance.

III. Antenna and Pylon Geometry

The fully assembled structure of a single dipole antenna element is highlighted in Fig. 1. The as-installed array consists of four elements (two on each wing) located at wing stations ±44 and ±86. As Fig. 1 shows, the antennas are dipole elements consisting of two arms that are 2.0" inches in diameter and a total length of 78.5". The arms of the antenna are oriented with the flight direction. The dipole is mounted to existing hardpoints on the UAS wing via a custom pylon structure. The pylon has a similar internal structure to a traditional wingbox with internal spars and ribs, while the external skin consists of mainly fiberglass. The antenna receives power through a feed that runs through the pylon to a matching network centered above the arms.

It is imperative to electrically isolate the arms from metallic elements of the structure to prevent shorting the arms of the dipole. This was achieved by shielding the arms with a fiberglass sleeve. As the antenna is comprised of two separate arms, these sleeves serve a secondary purpose of reinforcing the central section against bending. For further isolation, fiberglass spacers were also placed in between the lower spars and the lower rib. Finally, as the lower spars had to be fastened to the lower rib, the fasteners and nuts were isolated with a nylon shoulder washer.

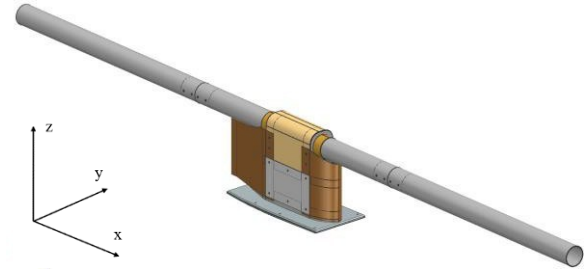

(a) Assembly

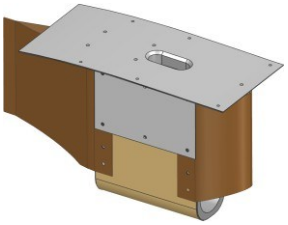

(b) Pylon

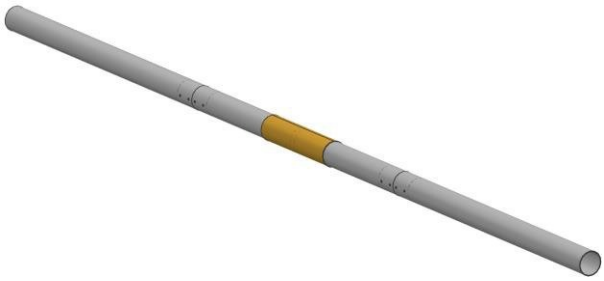

(c) Antenna

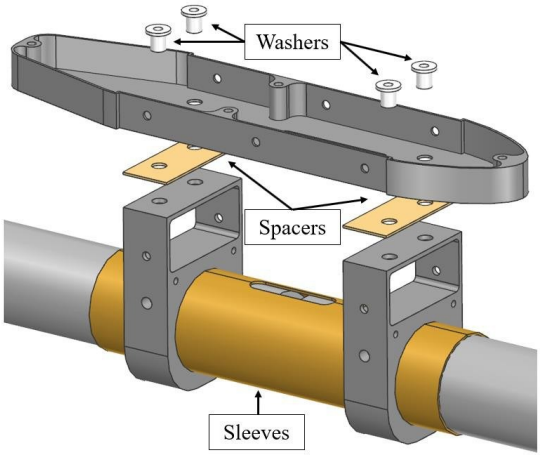

(d) Electrical Isolation Measures

Fig. 1 Geometry Overview

IV. Finite Element Model and Experimental Validation

A. Description of Finite Element Model

The first step in this study was to determine the natural frequencies and frequency response of the antenna when installed on the vehicle. A finite element model (FEM), illustrated in Fig. 2a, was constructed in MSC Patran. The FEM uses exclusively shell elements (CQUAD4) with isotropic property sets for metallic subcomponents (such as the antenna arms) and composite property sets for fiberglass components as shown in Fig. 2b. In this figure, red and dark blue sections of the antenna tube are composed of 6061-T6 aluminum with thicknesses of 0.049" and 0.089", respectively. The thicker section consists of an internal cuff that the antenna tube slides over. The boundary conditions for modal analysis, highlighted in red in Fig. 2c, are fixed translation constraints to simulate the structure as mounted to a wing. Specifically, z-translation is constrained at the border of the mount plate while translation in all three axes is constrained at fastener locations. The total degrees of freedom for the constrained model are 131,488. First a modal analysis was conducted with the model, and after validating the model with experimental results, the frequency response of the structure was simulated by using accelerations previously measured at the vehicle hardpoints by the Original Equipment Manufacturer (OEM).

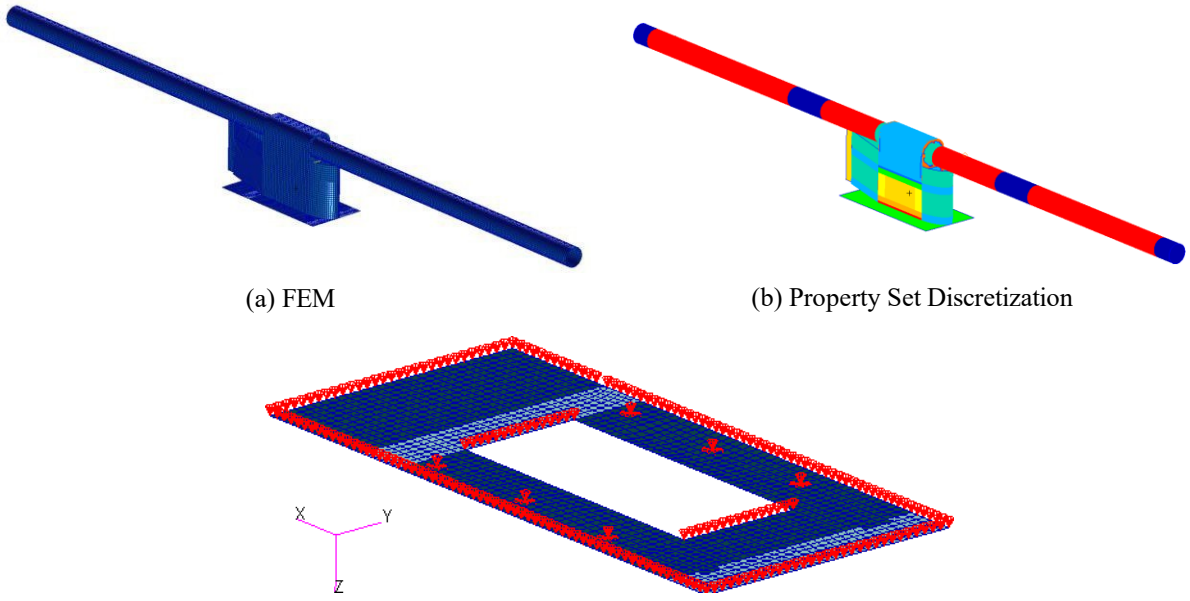

(a) FEM (b) Property Set Discretization

(a) Boundary Conditions

Fig. 2 FEM Overview

The response of the structure to external accelerations was modeled using NASTRAN solution sequence 111, which solves for the response by uncoupling the equations of motion by utilizing the normal modes of the structure. It is in general a more computationally efficient method than solution sequence 108 which directly solves the equations of motion. The first 20 normal modes in a specified frequency range of 0-400 Hz were calculated with the Lanczos algorithm for eigenvalue extraction. These parameters are expected to provide a satisfactory approximation of the true response, as the majority of the energy input into the system is at frequencies far less than 400 Hz.

External excitations were modeled using the power spectral density (PSD) of in-flight accelerometer data at hardpoint locations previously measured by the OEM. Given the PSD of a signal, the amplitude spectral density (ASD) is taken as the square root of PSD [7]. The ASD of the measured accelerations at the interior wing hardpoint during cruise was utilized as the input acceleration at the mount plate for the climb condition within Patran with phase randomized. Since engine RPM varies throughout flight, the BPF and associated harmonics are expected to shift as well. This effect is illustrated in Fig. 3 [8]. Note these values are purely for visualization and are not the as-measured harmonics from the vehicle.

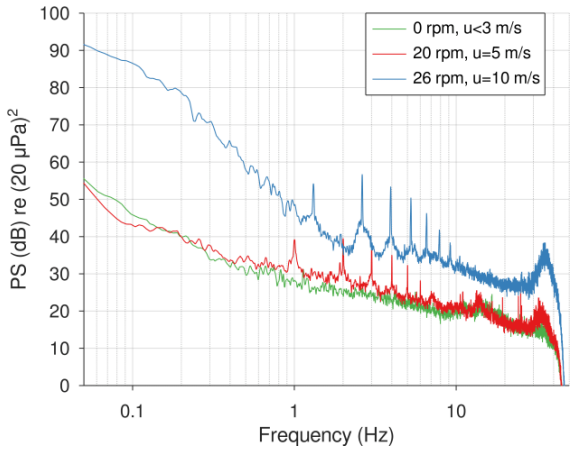

Fig. 3 Illustration of Effect of Variation in Engine RPM on BPF Harmonics [8]

V. Experimental Setup

B. Modal Test

To help verify the FEM results and to ensure that the natural modes of the wing-mounted antenna do not occur at the same frequencies as the engine RPM and blade passage frequency, a modal test was conducted in the lab. A schematic of the experimental setup is shown in Fig. 4. The data acquisition (DAQ) and post-processing was conducted through Data Physics SignalCalc 900 v2.1, while modal parameter extraction was done with ME'scopeVES v5.0. All accelerometers measured accelerations in the x-z plane of the structure as defined in Fig. 1a. The structure was excited at the point defined in Fig. 4 with a shaker. Simultaneous data collection at all points of interest is not possible due to channel limitations, so accelerometers are roved between tests to acquire data at all points, while the shaker location remains stationary. The initial accelerometer layout is shown in Fig. 5a. To mitigate rigid body motion and vibration of the mount plate, the structure was mounted to a 3D printed support with curvature matching the plate and then hard mounted to the table.

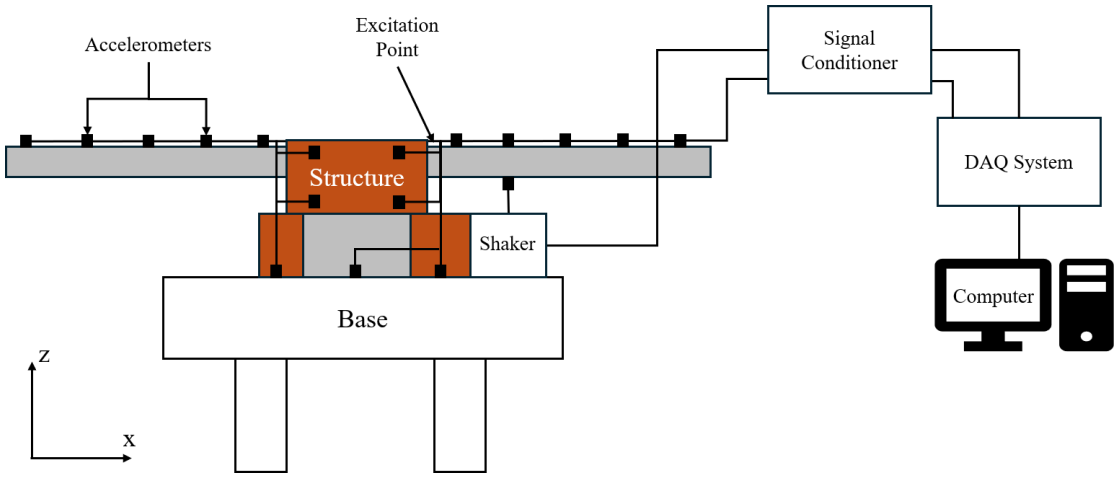

Fig. 4 Wiring Schematic

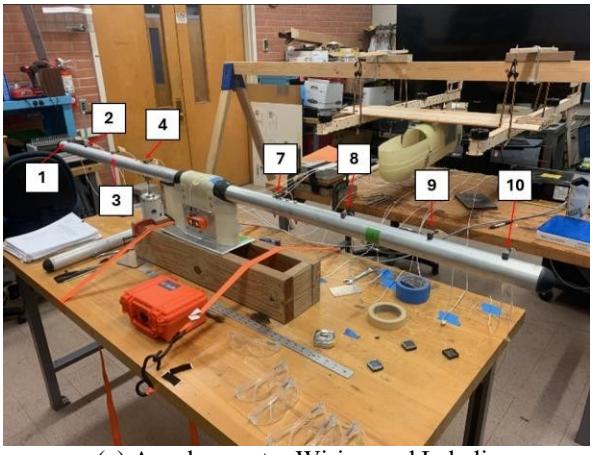

(a) Accelerometer Wiring and Labeling

(b) Mount Plate Support

Fig. 5 Experimental Modal Testing Setup

C. Comparison of FEA Results and Experimental Measurements

It is imperative to validate the FEM before performing subsequent analysis on the radar data collected during the flight test. The experimental modal test data is sparse due to the fact that only a single point was excited with the shaker. Measurements of the frequency response functions (FRFs) presented in Fig. 6 consist purely of the antenna arms, meaning no motion of the pylon is recorded. The first five natural frequencies identified for analysis were determined with curve-fitting.

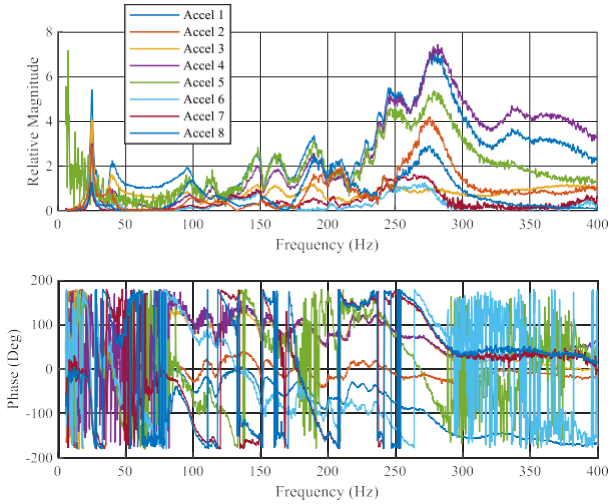

Fig. 6 FRFs Along Span of Antenna Arms

The first five normal modes from the FEM are compared with the first five mode shapes from the experimental results in Table 1. The results show that modes 1 and 2 were likely to be the nearest resonant frequencies to be excited during flight. It should be noted that several closely separated modes near mode 2 predicted from simulation were not identified in the experiment due to inadequate frequency resolution. Besides this minor exception, the experimental normal modes are in general in agreement with those determined by simulation. In particular, the lower frequency modes (Modes 1 and 2) are within 7 Hz, and these modes are expected to have the most significant impact on the radar signal.

Table 1 Comparison of FEM and Experimental Normal Modes

FEM Mode Shapes		Experimental Mode Shapes	
Freq. (Hz)	**Mode Shape**	**Freq. (Hz)**	**Mode Shape**
27	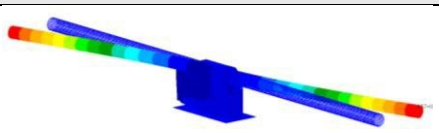	**25**	**Half Sine Wave Antisymmetric**
32.9	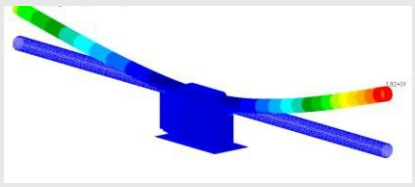	**39**	**First Bending (YZ-Plane)**
213	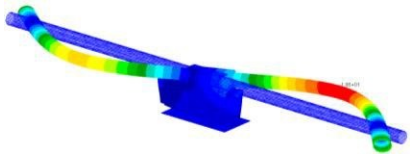	**186**	**Second Bending (YZ-Plane)**
249	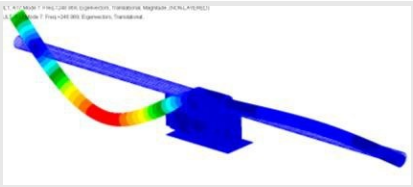	**273**	**Third Bending (XZ-Plane) Rear Arm Excited**
255	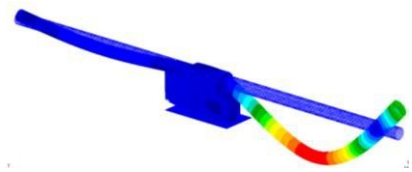	**276**	**Third Bending (XZ-Plane)**

With the FEA model validated, the response of the outboard-most antenna was simulated using the PSD input provided by the OEM for three flight conditions: climb, cruise, and descent. The distinction is made between these three phases of flight due to the differences in engine RPM and thus BPF harmonics. A comparison of engine RPM with both GPS and radar derived altitude readings from the flight test is presented in Fig. 7 to illustrate the differences between these conditions. The engine RPM associated with each phase of flight was determined to be 26 Hz, 23 Hz, and 18 Hz for climb, cruise, and descent respectively labeled as points A, B, and C. These rotational frequencies are maintained for an extended period of time during each phase of flight, allowing enough time for the effects of separate engine frequencies to damp out. While there is no consistent engine RPM across the entirety of the descent, a value of 18 Hz was chosen since it is fairly separated from the frequencies selected to represent climb and cruise.

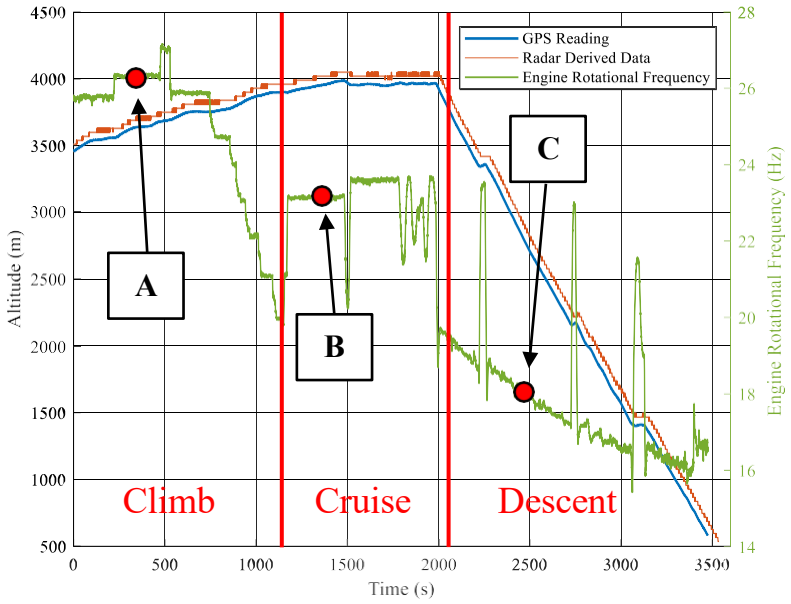

Fig. 7 Comparison of Three Phases of Flight

The PSD curves provided for the vehicle were measured during vehicle climb, so for cruise and descent simulations the PSDs were modified. The amplitude of resonant peaks were assumed to remain constant while the frequencies and associated harmonics were shifted down to the values identified previously. The relevant output from this sensitivity analysis is the displacement of the phase center as a function of frequency, as this is the apparent source of radiation that is referenced in post-processing of radar data. Variations in phase center displacement across the three phases of flight are compared in Fig. 8.

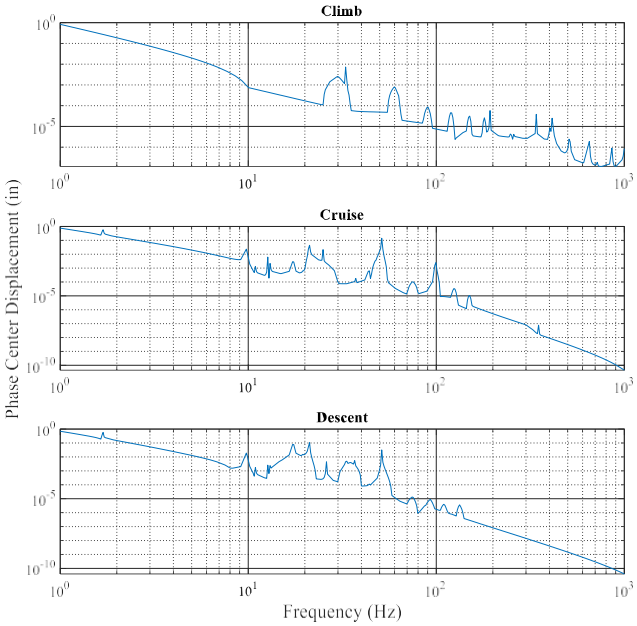

Fig. 8 Variations in Simulated Phase Center FRFs Across Flight

For all phases of flight, the largest predicted magnitude of displacement occurs at frequencies less than 10 Hz due to rigid body motion of the mount plate. The observed differences in resonance peaks between different phases of flight are primarily due to the variation in input frequencies either amplifying or negating the natural frequencies of the antenna. The largest resonance peak occurs in the cruise condition at 1.7 Hz with a maximum displacement of 0.58 in., and the second largest occurs at 26 Hz with an amplitude of 0.18 in. during cruise as well. These displacements may be small relative to the oscillation of the UAS due to dynamic mode excitations, but this local effect has been shown in previous work to be observable [9].

VI. In-Flight Radar Measurements

D. Flight Test

For the as-flown system, four antennas were installed at preexisting hardpoint locations along the wingspan of the UAS as shown in Fig. 9. A flight test of the system was conducted in the Fall of 2024 over open water so the radar return is that of a specular target (at these low frequencies waves are small and negligible). The flight was approximately 4.5 hours long, and radar data began being collected after 2.8 hours at an altitude of 11,400 ft. During the measurements the aircraft climbed from 11,400 ft to 13,100 ft at an average climb rate of 66 fpm. It remained at this altitude for approximately 8 minutes, then descended to 1,640 ft over the course of 25 minutes after which the radar was turned off. During the climb and descent, the vehicle flew a racetrack pattern with legs approximately 10 miles long.

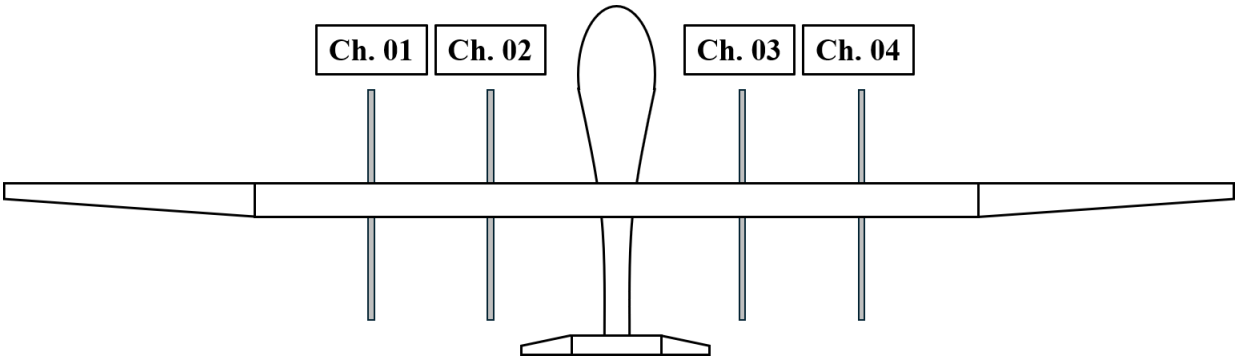

Fig. 9 Channel Numbering Scheme

E. In-Flight Radar Measurements

To investigate the effects of the mechanical vibrations on the radar signal, the phase and magnitude of the reflected signal will be examined. As the antenna moves up and down due to the vibrations, it is expected that the phase of the return signal will vary at a similar rate. This is due to the incrementally longer/shorter distance the signal would need to travel. Furthermore, previous work has shown that the magnitude of the signal will also vary based on mechanical vibrations [9].

A time domain sample of the radar signal during the climb phase of the flight is shown on the left side of Fig. 10, and the fast Fourier transform (FFT) of the same signal is presented on the right in Fig. 10. Similar results for both cruise and descent are displayed in Fig. 11 and Fig. 12, respectively. To account for the expected phase changes due to the ascent or descent of the vehicle, the phase is unwrapped and the least-squares line is subtracted from the phase data before taking the FFT. The phase unwrapping prevents phase discontinuities from masking smaller signals and the trend line subtraction filters out the rigid body motion of the UAS.

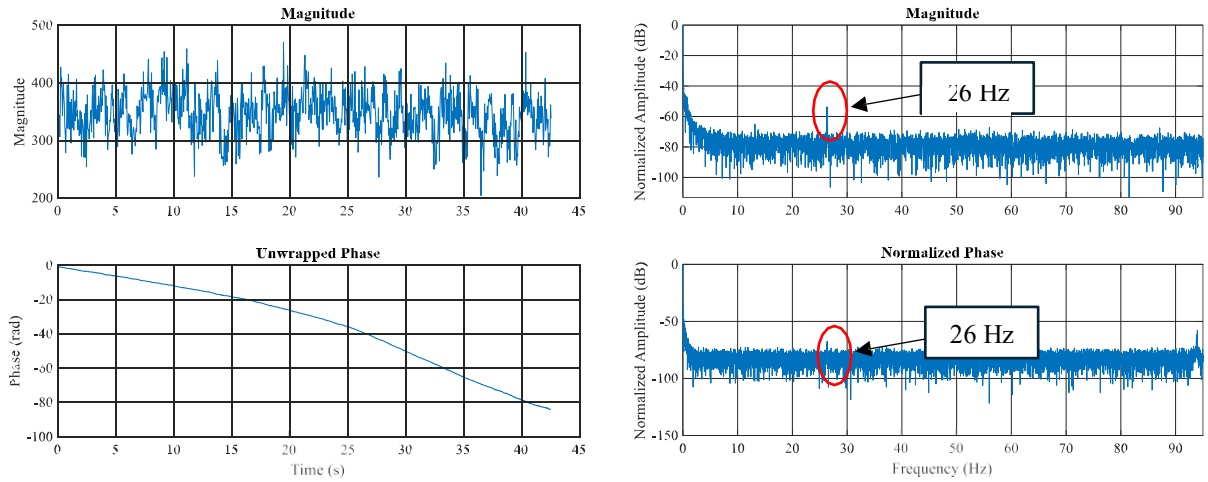

(a) Time Domain (b) Frequency Domain

Fig. 10 Ch. 01 Return Magnitude and Phase at Point A (Climb)

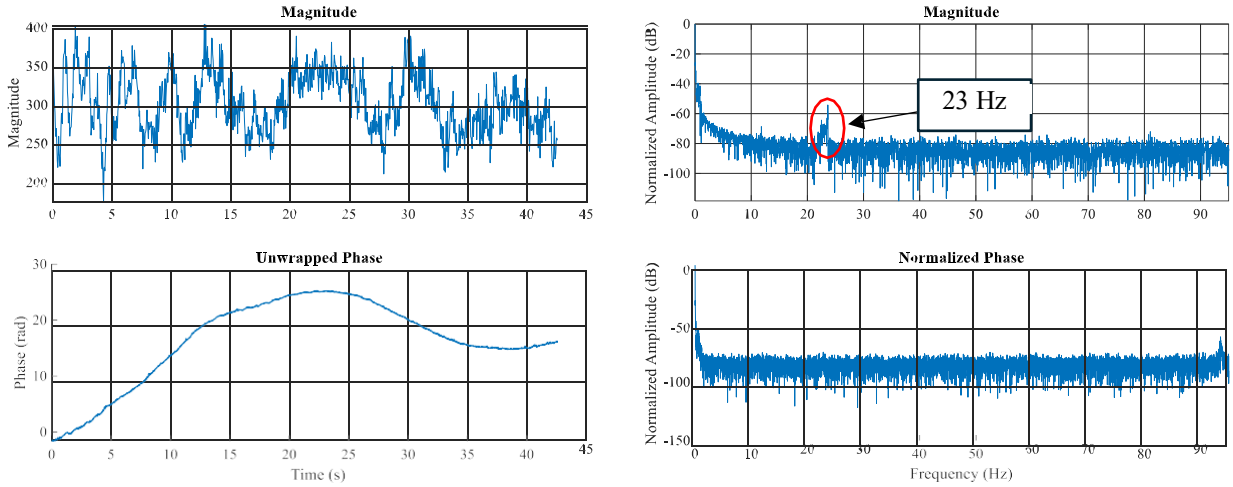

(a) Time Domain (b) Frequency Domain

Fig. 11 Ch. 01 Return Magnitude and Phase at Point B (Cruise)

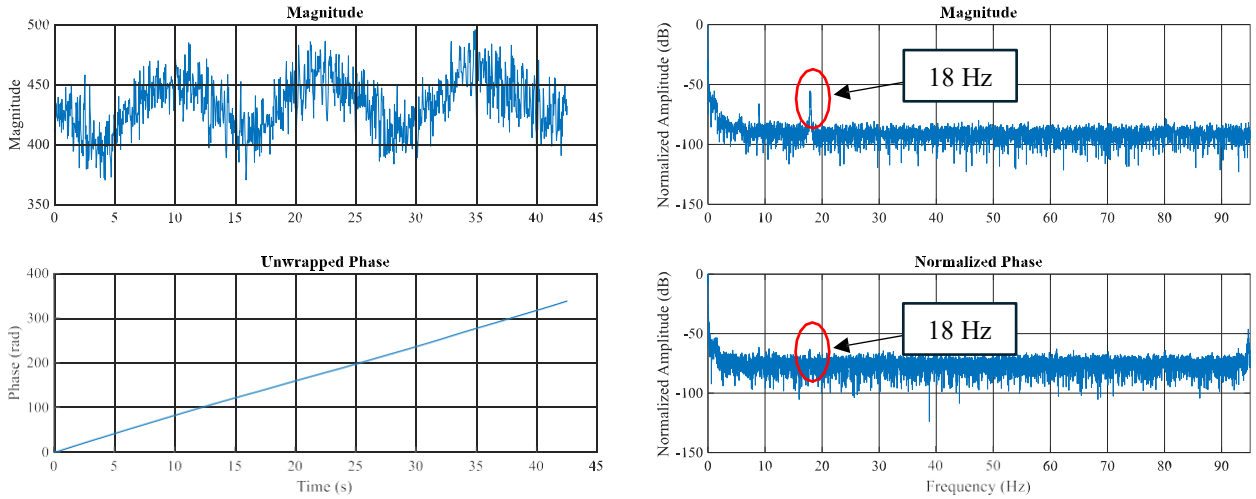

(a) Time Domain (b) Frequency Domain

Fig. 12 Ch. 01 Return Magnitude and Phase at Point C (Descent)

Across all phases of flight, a significant fraction of the total energy is concentrated at or below 2 Hz. This is suspected to be a result of rigid body motion and/or dynamic mode excitation of the aircraft. During climb, it is evident that the engine RPM has a noticeable effect on the magnitude and to a lesser extent the phase of the signal, with the most prominent peak occurring exactly at the engine frequency of 26 Hz (point A in Fig. 7). Subharmonic peaks of engine RPM are observed in the magnitude of the radar signal across all phases of flight, but higher order BPFs do not appear to significantly contribute to the radar signal in any form nor do the local modes of the antenna structure.

Wing vibrations due to the engine have a clear effect on the magnitude of the signal as the shift in the frequency domain peak location across the three flight phases clearly correlates with a change in engine RPM. This claim is further supported by examining a time period during descent when the UAS briefly levels out to perform a coordinated turn. During this maneuver engine RPM increased from 19 to 24 Hz as evident by a sharp peak in RPM during the descent phase in Fig. 7. Fig. 13 illustrates the peak in the radar data broadening across this frequency range. This peak broadening is not present in the phase of the signal, although there is an identifiable peak at 19 Hz.

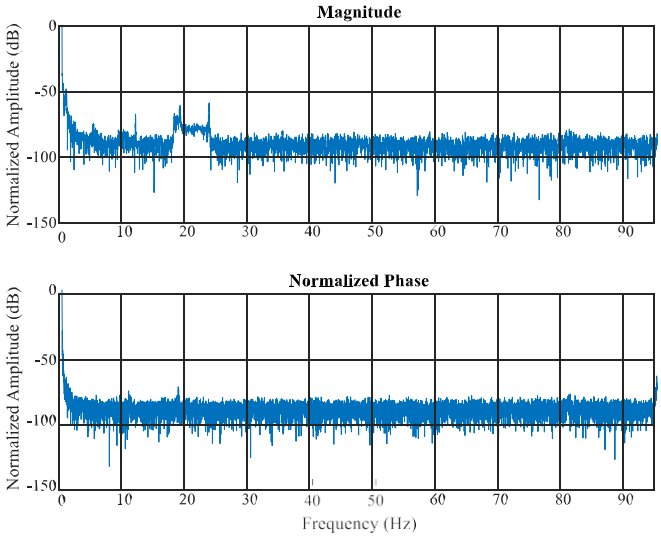

Fig. 13 Peak Broadening due to Coordinated Turn Maneuver

In contrast to work done by Arnold et al. [9], the effects of in-flight vibrations are most prominent in the magnitude of the return signal. It was initially hypothesized that phase changes due to deformation of the wing would be the dominant effect as was the case in lab testing. Although present, the phase variations are minor in comparison to magnitude variations. Note the magnitude variations were still present in lab testing, but not to the extent found during the flight test. Further study is recommended to characterize this effect.

Harmonics of BPF observed in simulations do not appear to have a meaningful effect on radar data either. It is likely that the energy content of these higher order harmonics are negligible in comparison to the fundamental frequency of the engine. Again, this finding supports that the primary source of magnitude and phase errors is caused by the engine RPM.

VII. Conclusions

This study examined how the mechanical vibrational response of wing-mounted 70 MHz antennas used for an ice-sounding radar system impacts the radar signal. Local dynamic modes of the antenna were first assessed using an FEA model and validated with experimental measurements. The response of the antenna to expected in-flight vibrations was then assessed using the same FEA model and an FRF input extracted from previous measurements of the wing hardpoints. Radar data from a recent flight test of the system was then used to examine whether the mechanical modes of the antenna and structure are apparent. Simulations of in-flight vibrations predicted that this particular system experienced the largest antenna displacements due to rigid body motion of the wing, while specific flight conditions, such as cruise, exacerbate resonance at certain frequencies due to engine and BPF harmonics. The results demonstrated that mechanical vibrations, particularly those occurring at the engine frequencies, had measurable influence on the magnitude of the radar signal. This was confirmed by analysis of in-flight radar data. No other prominent frequencies were apparent in the magnitude data, other than those associated with the engine vibrations. This suggests that the dominant effect on the radar signal is caused by the vibration of the wing, rather than local modes of the antenna arms. Rather unexpectedly, the mechanical vibrations were less apparent in the phase data. While small peaks were observed at the engine frequencies for climb and descent phases, no peak was observed during cruise. Even when peaks were observable, only in the context of the magnitude response would one likely recognize them. In [9], mechanical vibrations were observed in both the phase and magnitudes of a radar signal. In the present study, even when the engine frequencies were observed in the phase data, the magnitude was very small. One follow-up analysis that must be conducted is verifying the effects of the vibrations on the radar electronics themselves. In this case, the radar chassis was mounted in the nose of the aircraft. While the UAS is a pusher configuration, the radar electronics will also experience the vibrations of the airframe. As follow-on work, we plan to shake the radar electronics in the lab to verify that the vibrations do not cause magnitude errors in the electronics.

The next steps of this work include examining how these phase and magnitude errors in the radar signal affect beamforming capabilities of the array. Coherent radars used in ice sounding rely on advanced beamforming algorithms to help suppress clutter signals. Even small errors in amplitude and phases can affect the accurate placement of beam nulls. Finally, we also hope to examine whether vibration isolation techniques can help mitigate the adverse effects of in-flight vibrations. Future efforts should also explore not only damping mechanisms, but signal-processing techniques as well.

Acknowledgements

This work was funded by NSF grant 2216455. The authors would like to acknowledge the contributions of our many CReSIS colleagues in developing the radar system and antennas. These colleagues include Carl Leuschen, Fernando Rodgriguez-Morales, Daniel Gomez-Garcia, Aaron Paden, Master's student Sam Ross, Brad Schroeder, and William Gobel. We would also like to thank Jilu Li and John Paden in their contributions related to processing the raw radar data. We would also like to thank our industry colleagues as well as Fernando Rodriguez-Morales and PhD student Shravan Kaundinya in supporting the flight test activities.

References

[1] E. Arnold, C. Leuschen, F. Rodriguez-Moralez, J. Li, R. Hale and S. Keshmiri, "CReSIS Airborne Radars and Platforms for Ice and Snow Sounding," *Annals of Glaciology,* no. 81, pp. 1-10, 2019.

[2] E. Arnold, F. Rodriguez-Morales, J. Paden, C. Leuschen, S. Keshmiri, S. Yan, M. Ewing, R. Hale, A. Mahmood, A. Blevins, A. Mishra, T. Karidi, B. Miller and J. Soontag, "HF/VHF Radar Sounding of Ice from Manned and Unmanned Airborne Platforms," *Geosciences,* vol. 8, no. 5, May 2018.

[3] K. Lindbäck, R. Pettersson, S. H. Doyle, C. Helanow, P. Jansson, S. S. Kristensen, L. Stenseng, R. Forsberg and A. L. Hubbard, "High-reslolution ice thickness and bed topography of a land-terminating section of the Greenland Ice Sheet," *Earth System Science Data,* vol. 6, no. 2, pp. 331-338, 2014.

[4] U. Nixdorf, D. Steinhage, U. Meyer, L. Hempel, M. Jenett, P. Wachs and H. Miller, "The newly developed airborne radio-echo sounding system of the AWI as a glaciological tool," *Annals of Glaciology,* vol. 29, pp. 231-238, 1999.

[5] M. E. Peters, D. D. Blankenship, S. P. Carter, S. D. Kempf, D. A. Young and J. W. Holt, "Along-Track Focusing of Aircorne Radar Sounding Data from West Antarctica for Improving Basal Reflection Analaysis and Layer Detection," *IEEE Transactions on Geoscience and Remote Sensing,* vol. 45, no. 9, pp. 2725-2736, September 2007.

[6] J. W. Burns, E. J. Arnold and U. Ballingu, "Weight-Optimized Structural Antenna Concept for UAS Remote Sensing," in *AIAA SciTech 2022 Forum*, San Diego, 2022.

[7] M. Cerna and A. Harvey, "The Fundamentals of FFT-Based Signal Analysis and Measurement," National Instruments Corporation, 2000.

[8] C. Pilger and L. Ceranna, "The influence of periodic wind turbine noise on infrasound," *Journal of Sound and Vibration,* vol. 388, pp. 188-200, 2017.

[9] E. Arnold, J. B. Yan, R. Hale, F. Rodriguez-Morales, P. Gogineni, J. Li and M. Ewing, "Effects of Vibration on a Wing-Mounted Ice Sounding Antenna Array," *IEEE Antennas and Propegation,* vol. 56, no. 6, pp. 41-52, December 2014.